# An Innovative Experimental Approach to Lateral-Directional Flying Quality Investigation for Tailless Aircraft

Bowen Nie, Zhitao Liu, Fei Cen, Duoneng Liu, Hongxu Ma, Olivier Sename

## To cite this version:

Bowen Nie, Zhitao Liu, Fei Cen, Duoneng Liu, Hongxu Ma, et al.. An Innovative Experimental Approach to Lateral-Directional Flying Quality Investigation for Tailless Aircraft. IEEE Access, 2020, 8, pp.109543-109556. ⟨10.1109/ACCESS.2020.3001913⟩. ⟨hal-02917902⟩

IEEE Access
Multidisciplinary ⋮ Rapid Review ⋮ Open Access Journal

Received May 27, 2020, accepted June 8, 2020, date of publication June 12, 2020, date of current version June 24, 2020.

*Digital Object Identifier 10.1109/ACCESS.2020.3001913*

# An Innovative Experimental Approach to Lateral-Directional Flying Quality Investigation for Tailless Aircraft

**BOWEN NIE [1,2], ZHITAO LIU [2], FEI CEN [2], DUONENG LIU [2], HONGXU MA [1], AND OLIVIER SENAME [3]**

[1]College of Intelligence Science and Technology, National University of Defense Technology, Changsha 410073, China
[2]Low Speed Aerodynamics Institute, China Aerodynamics Research and Development Center, Mianyang 621000, China
[3]GIPSA-Lab, CNRS, Grenoble INP (Institute of Engineering, Université Grenoble-Alpes), 38000 Grenoble, France

Corresponding author: Bowen Nie (niebowen_cardc@outlook.com)

**ABSTRACT** Tailless aircraft suffers from limited yaw control power and poor directional stability inherently. To address these issues in the early design process of a tailless configuration with low costs and risks, this paper presents an innovative experimental approach to control law validation and quantitative flying quality evaluation with a dynamically scaled model mounted on a three degree-of-freedom rig in the wind tunnel. The motion equations of the tailless demonstrator on the rig are derived, and then the comparisons of the lateral-directional flight dynamics between the rig constrained model and the free flight model are carried out. Construction of the control augmentation system for yaw and roll motion is accomplished according to the scale modified criteria of flying qualities. Effectiveness of the designed control law is demonstrated with steady pilot-in-the-loop flights at different airspeeds and angles of attack. The achieved closed-loop flying qualities are evaluated by applying multistep maneuvers for low order equivalent system identification. Whereas severe instability is observed in yaw for the open-loop case, the closed-loop flying quality of the Dutch-roll mode can be improved to level 1 at low angle of attack.

**INDEX TERMS** Tailless aircraft, dynamic rig, wind tunnel, semi-free flight test, control law validation, flying quality evaluation.

## I. INTRODUCTION

Tailless aircraft has regained much research interest over the last decades. A significant reduction of radar signature and fuel consumption makes the tailless configuration one of the most promising candidates for future generation military and civil aircraft [1], [2]. However, the stealth-bound tailless configurations are always associated with limited yaw control power, multi-axis instability, and highly nonlinear coupled control effectors [3]. To reduce the development costs and risks of a tailless aircraft drastically, these key issues should be identified and addressed earlier in the design process [4], [5].

From a stability and control point of view, wind tunnel experiment is still an indispensable approach to generate the aerodynamic dataset and construct the flight dynamic model of tailless aircraft prior to the costly flight test phase, even though it suffers from the issues of model scaling and difficulty of unsteady behavior simulation. To predict the static and dynamic stability and control characteristics of the tailless SACCON (stability and control configuration) configuration with an integrated computational and experimental approach, a series of static and forced-oscillation tests were conducted to form a basis for computational fluid dynamics (CFD) code validation [6], [7]. Similarly, validation of the variable-fidelity aerodynamic analysis result was carried out using existing wind tunnel data of the tailless ICE (innovative control effectors) 101 configuration, and eigenvalue analysis was then performed to the open-loop system matrices [8]. Weak instabilities were observed in some of the flight modes, especially in the sideslip condition, which could be easily controlled by the control effectors. Besides the conventional linear evaluation methods [9], a novel approach of identifying the aerodynamic model from innovative wind tunnel maneuvers was employed for the tailless DLR-F19 configuration [10], [11]. The resulting aerodynamic model was

The associate editor coordinating the review of this manuscript and approving it for publication was Halil Ersin Soken.

able to capture the highly nonlinear aerodynamic effects and could directly be integrated into the flight dynamics model, which exhibited Dutch-roll mode corresponding to flying qualities worse than level 3. Not surprisingly, low directional stability and yaw damping ratio are expected for the tailless configurations due to an absence of vertical and horizontal stabilizers, active flight control systems are normally required to accomplish the desired flying qualities. Hence, there has been an increasing need to extend wind tunnel tests to validate and evaluate the control schemes for tailless aircraft.

However, to the authors' best knowledge, there are few investigations for closed-loop flight tests on tailless configurations in the wind tunnel in recent years. A tailless model known as Swing [12]–[14] was supported upside down with a sting through the fuselage in the wind tunnel, which enabled the model to rotate freely in yaw. Classical control laws were designed and implemented to handle the directional instability at moderate sideslip angles, and a dynamic-recovery scheme was worked out to restore the aircraft from yaw departure at larger sideslip angles when static split-flap deflection was not effective enough. Moreover, a 5-percent scale model of the Boeing Blended-Wing-Body (BWB) configuration was flown within the Langley Full-Scale Tunnel (LFST) in all six degree-of-freedom (DOF), while equipped with control surface allocation and stability augmentation system [15], [16]. The results of the free flight test validated the designed control laws and indicated satisfactory flight behavior. One can see that the main idea is to allow the scaled tailless aircraft to fly in a wind tunnel working section freely or with partially constrained motion imposed by a dynamic rig [17], which has previously been used for identification and control investigations of conventional aircraft [18]–[22].

This paper aims at exploring the aforementioned dynamic rig to deal with lateral-directional control law validation of the tailless configurations with a particular focus on quantitative evaluation of flying qualities according to the scale modified criteria. The novelty of this work lies in the first combination of a 3-DOF dynamic rig and dynamically scaled tailless demonstrator in a pilot-in-the-loop (PIL) setup for control law validation and flying quality evaluation in the wind tunnel. It is not trivial to mention that the proposed validation and evaluation techniques can be integrated into an iterative design procedure of tailless aircraft with limited costs and risks.

This paper is organized as follows. Section II briefly introduces the tailless demonstrator along with the experimental setup. In Sec. III, flight dynamic model of the tailless demonstrator on the 3-DOF rig is derived, especially the construction of aerodynamic model with conventional wind-tunnel test data. In section IV, the influence of the 3-DOF rig to the flight dynamics is discussed via bifurcation analysis and nonlinear simulation. Section V deals with the design of control law using the Eigenstructure Assignment (EA) method. Finally, the designed control law is validated and evaluated on the experimental setup in Sec. VI.

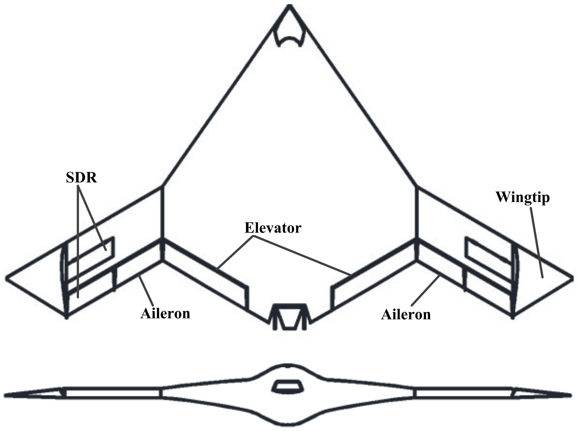

**FIGURE 1.** Sketch of the tailless demonstrator.

## II. AIRCRAFT MODEL AND EXPERIMENTAL SETUP

A schematic view of the tailless demonstrator is presented in Fig. 1. It's an aircraft with medium-aspect-ratio, double sweep and blended wing body configuration. In the tailless configuration, there are ten control surfaces including six trailing-edge flaps, two mid-wing spoilers and two wingtips that can be actuated individually with electrical servos. The two inner flaps are deflected with the same angle for pitch control. Asymmetric deflections with the same angle for the two intermediate flaps are used for roll control. Yaw control is achieved by the split drag rudder (SDR), namely, deflection with the same amplitude for the outer flap and the mid-wing spoiler on one wing. The wingtips can be fixed at a preselected deflection to improve directional stability at the expense of stealth. With respect to the airframe, the two inner flaps moving down is referred to as a positive elevator deflection, the intermediate flap on the left wing moving up and the right one moving down is referred to as a positive aileron deflection, the positive rudder deflection is defined as the outer flap goes down and the mid-wing spoiler goes up on the left wing, and positive wing tip is achieved when the two tips go up to the same deflection. A dynamically scaled model has been designed and manufactured for investigation of aerodynamics, stability and control laws in a low-speed wind tunnel, whose main physical parameters are listed in Table 1.

As shown in Fig. 2, the aircraft model can be supported at the center of gravity (CG) using a 3-DOF maneuver rig through the bottom of the fuselage to free the rotational motions and eliminate the translational motions. The rig is fixed to the floor in the test section of the FL-14 wind tunnel, and attached to the aircraft model with a spherical joint, which supplies sufficient attitude range (roll: ± 40°, pitch: ± 40° and yaw: ± 180° ) with high precision, high rigidity, and negligible frictional resistance [21], [22]. Besides the servo driving control surfaces, the aircraft model is also equipped with sensors, including two vanes for airflow angles ($\alpha$, $\beta$), an inertial measurement unit (IMU) for angular velocities ($p, q, r$) and an attitude & heading reference system (AHRS) for Euler angles ($\phi$, $\theta$, $\psi$). The onboard avionics are wired

**TABLE 1. Physical properties of the dynamically scaled aircraft model.**

| Name | Symbol | Value |
|---|---|---|
| Scale ratio | $K_L$ | 10% |
| Span | b | 2.0 m |
| Mean chord | $\bar{c}$ | 0.6571 m |
| Wing area | S | 0.8742 m$^2$ |
| Mass | m | 16.85 kg |
| Moment of inertia | $J_x/J_y/J_z$ | 1.1017/ 0.7380/ 1.6920 kg.m$^2$ |
| Elevator / Aileron deflection | $\delta_e$ / $\delta_a$ | ±30° |
| Rudder / Wingtip deflection | $\delta_r$ / $\delta_{wt}$ | ±40° |

**FIGURE 2.** Tailless aircraft model on the 3-DOF dynamic rig.

to the real-time controller, which locates outside the test section and performs control law operation, data acquisition and command allocation at a frequency of 100 Hz.

During the tests, the aircraft model is driven by the airflow and surface deflections to perform semi-free flights, namely rotate freely with respect to the center of the spherical joint, while the translational motions are eliminated by the rig. The flight control system acts as a stability augmentation system (SAS) or a control augmentation system (CAS) depending on the design of control law. A 'pilot' is required to handle the aircraft model with a stick, which is used to generate the reference commands for the control system. Subsequently, a pilot-in-the-loop (PIL) experimental setup is figured out via the integration of wind tunnel, aircraft model, dynamic rig, flight control system and pilot, which can be applied to validate and evaluate the control laws. It is important to mention that a researcher without the experience of handling a full-scale aircraft could also be adequate as the 'pilot' herein.

## III. MATHEMATICAL MODELING

In this section, the mathematical model of aircraft dynamics on the 3-DOF rig is derived considering the motion constraint, assembling misalignment and joint friction.

### A. DYNAMIC MODELING OF AIRCRAFT ON THE RIG

First of all, the following assumptions are made:

1) The tailless aircraft model is considered to be a rigid body.
2) Distribution of the tailless aircraft model's mass is symmetrical with respect to the longitudinal plane.
3) The aerodynamic interference induced by the 3-DOF rig is negligible.

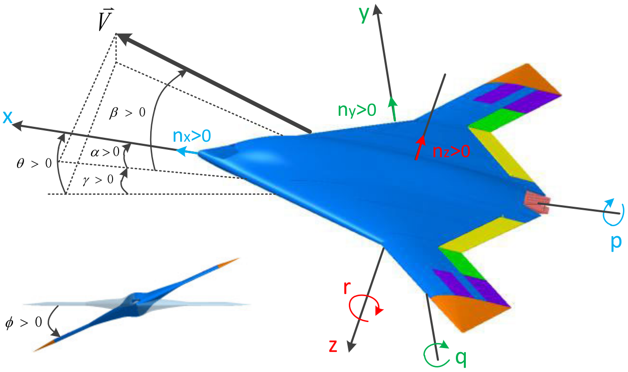

**FIGURE 3.** Definition of the coordinates and core states.

Two reference frames are used as depicted in Fig. 3, including the body-fixed and the wind-tunnel-fixed frames. The equations of motion for the aircraft model on the rig are derived and simplified based on the typical equations for a 6-DOF free flight [23], [24] as follows:

$$\dot{V} = 0 \tag{1a}$$

$$\dot{\alpha} = \frac{q\cos\beta - (p\cos\alpha + r\sin\alpha)\sin\beta}{\cos\beta} \tag{1b}$$

$$\dot{\beta} = p\sin\alpha - r\cos\alpha \tag{1c}$$

$$\dot{p} = \frac{J_{xz}}{J_x}\dot{r} - qr\frac{J_z - J_y}{J_x} + qp\frac{J_{xz}}{J_x} + \frac{L}{J_x} \tag{1d}$$

$$\dot{q} = -pr\frac{J_x - J_z}{J_y} - \left(p^2 - r^2\right)\frac{J_{xz}}{J_y} + \frac{M}{J_y} \tag{1e}$$

$$\dot{r} = \frac{J_{xz}}{J_z}\dot{p} - pq\frac{J_y - J_x}{J_z} - qr\frac{J_{xz}}{J_z} + \frac{N}{J_z} \tag{1f}$$

$$\dot{\phi} = p + \tan\theta\,(p\sin\phi + r\cos\phi) \tag{1g}$$

$$\dot{\theta} = q\cos\phi - r\sin\phi \tag{1h}$$

$$\dot{\psi} = \sec\theta\,(q\sin\phi + r\cos\phi) \tag{1i}$$

where $(V, \alpha, \beta)$ are the aerodynamic states, namely, true airspeed, angle of attack and angle of sideslip, the states $(p, q, r)$ correspond to the angular rates along the body axes, meanwhile the states $(\phi, \theta, \psi)$ denote the attitude of roll, pitch, and yaw. The moments of inertia $J_x, J_y, J_z$ and the cross moment of inertia $J_{xz}$ are supposed to be constants. Herein, the path angle $\gamma$ is fixed at zero by the steady airflow in the test section of the wind tunnel during the flight tests, and the load factors $\left(n_x, n_y, n_z\right)$ are not available via the inertial sensors because the translational motions of the aircraft model are eliminated by the rig.

Though there is a hole on the fuselage's underside for rig support with sufficient maneuver range, the gap between model and rig is minimized beforehand to fit the flight states and reduce the aerodynamic interference. Subsequently, the aerodynamic interference from the rig is not taken into account as the previous studies [13], [18]–[21]. As a result, the external moments $(L, M, N)$ in the body-fixed reference frame about the CG can be decomposed into three terms:

$$\begin{aligned} L &= L_a + L_{cg} + L_f \\ M &= M_a + M_{cg} + M_f \\ N &= N_a + N_{cg} + N_f \end{aligned} \tag{2}$$

The subscript *a, cg, f* denotes aerodynamic actions, misalignment of the CG with respect to the center of the spherical joint, and rig friction, respectively.

### B. AERODYNAMIC MODELING

The aerodynamic moments are generally given by

$$L_a = \bar{q}SbC_l, \quad M_a = \bar{q}S\bar{c}C_m, \; N_a = \bar{q}SbC_n \tag{3}$$

in which $C_l, C_m, C_n$ are dimensionless coefficients for the aerodynamic moments, whereas $S, b, \bar{c}$ denote the reference wing area, wingspan and mean aerodynamic chord, respectively.

For attached flows at low angle of attack, $C_l, C_m, C_n$ are usually approximated by a sum of terms as following [23]:

$$\begin{aligned} C_l = {} & C_{l0}(\alpha, \beta) + \hat{C}_{l_p}(\alpha)\,\widehat{p} + \hat{C}_{l_r}(\alpha)\,\widehat{r} \\ & + \Delta C_{l_{\delta_a}}(\alpha, \beta, \delta_a) + \Delta C_{l_{\delta_r}}(\alpha, \beta, \delta_r) + \Delta C_{l_{wt}}(\alpha, \beta) \end{aligned} \tag{4a}$$

$$C_m = C_{m0}(\alpha) + \hat{C}_{m_q}(\alpha)\,\widehat{q} + \Delta C_{m_{\delta_e}}(\alpha, \delta_e) + \Delta C_{m_{wt}}(\alpha, \beta) \tag{4b}$$

$$\begin{aligned} C_n = {} & C_{n0}(\alpha, \beta) + \hat{C}_{n_p}(\alpha)\,\widehat{p} + \hat{C}_{n_r}(\alpha)\,\widehat{r} \\ & + \Delta C_{n_{\delta_a}}(\alpha, \beta, \delta_a) + \Delta C_{n_{\delta_r}}(\alpha, \beta, \delta_r) + \Delta C_{n_{wt}}(\alpha, \beta) \end{aligned} \tag{4c}$$

The components depend on the angle of $\alpha$ and $\beta$, the normalized body rates $\hat{p} = pb/2V$, $\hat{q} = qq\bar{c}/2V$, $\hat{r} = rb/2V$, as well as the surface deflections, including the elevator $\delta_e$, aileron $\delta_a$, rudder $\delta_r$, and wingtip $\delta_{wt}$. The nonlinear aerodynamic functions $C_{i_j}$ with $i = \{l, m, n\}$ and $j = \{\alpha, \beta, p, q, r, \delta_e, \delta_a, \delta_r, \delta_{wt}\}$ are obtained from the conventional steady and forced-oscillation tests in the FL-14 wind tunnel using a strain gauge balance.

The lack of a conventional vertical tail makes yaw stability and control quite challenging. Thus, in the early design process of this tailless configuration, the modeling emphasis is placed on yaw and roll moments for the incidence range from $-5°$ to $20°$ and sideslip range from $-12°$ to $12°$.

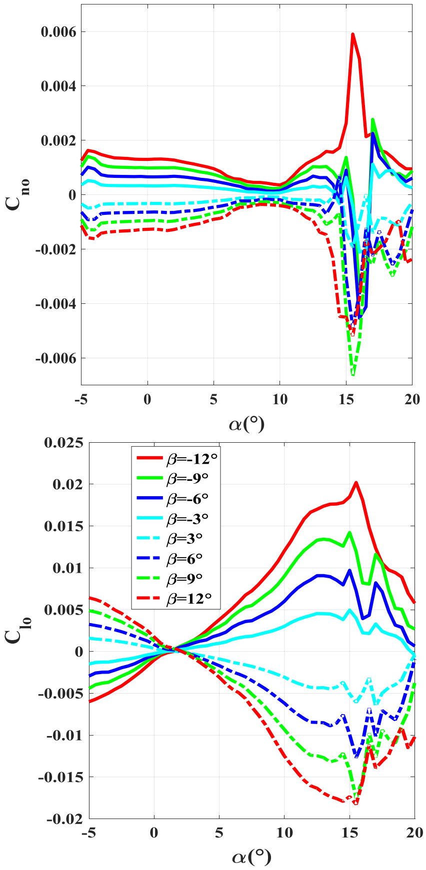

**FIGURE 4.** Baseline yaw & roll moments with respect to $\alpha$ and $\beta$.

As presented in Fig. 4, the baseline static coefficients $C_{n0}(\alpha, \beta)$ and $C_{l0}(\alpha, \beta)$ are determined along $\alpha$ at different $\beta$ with zero surface deflection in static wind tunnel tests. Recalling that static stability in yaw is defined as $C_{n\beta} = \partial C_n / \partial \beta > 0$. Hence, for positive $\beta$ (nosing to the left), the yawing moment should be positive to restore the aircraft to symmetric flight. It is noted that the tailless demonstrator is unstable in yaw at low $\alpha$, while the dihedral derivative $(C_{l_\beta} = \partial C_l / \partial \beta < 0)$ achieves positive stiffness. A slight decrease of directional instability at higher $\alpha$ is observed in the subsection from about 5° to 10°. However, with further increase of $\alpha$, nonsymmetrical moments and deterioration of directional stability arise, probably, due to flow separation on the wings. Beyond the stall angle of attack $\alpha_{cr} \approx 15°$, the nonlinearity and asymmetry burst in the yaw and roll moments.

The combined dynamic derivatives $\hat{C}_{n_r}, \hat{C}_{n_p}, \hat{C}_{l_p}, \hat{C}_{l_r}$ are obtained by performing forced-oscillation tests with different amplitudes and frequency at a series of $\alpha$ for several $\beta$. It is found from the experimental data that the nonlinearity is mainly dependent on $\alpha$, as presented in Fig. 5. The values of

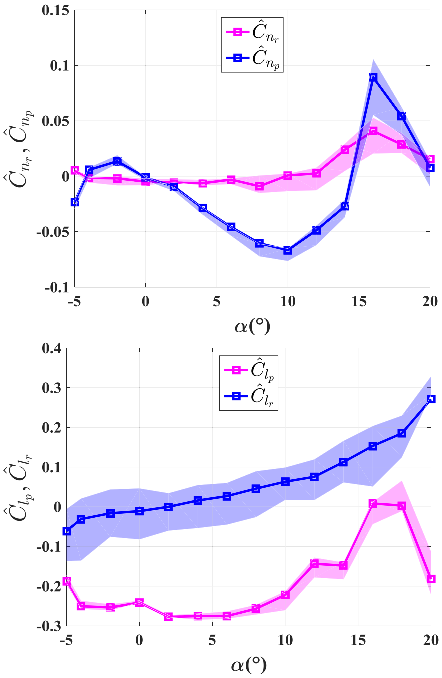

**FIGURE 5.** Lateral-directional dynamic derivatives.

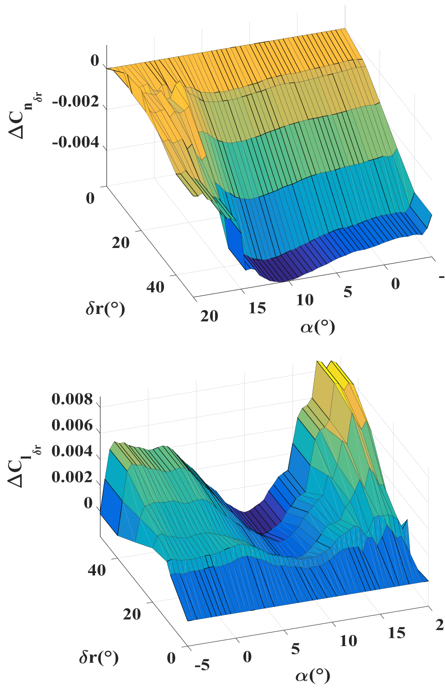

**FIGURE 6.** Increment of lateral-directional coefficients for $\delta_r$ at $\beta = 0^o$.

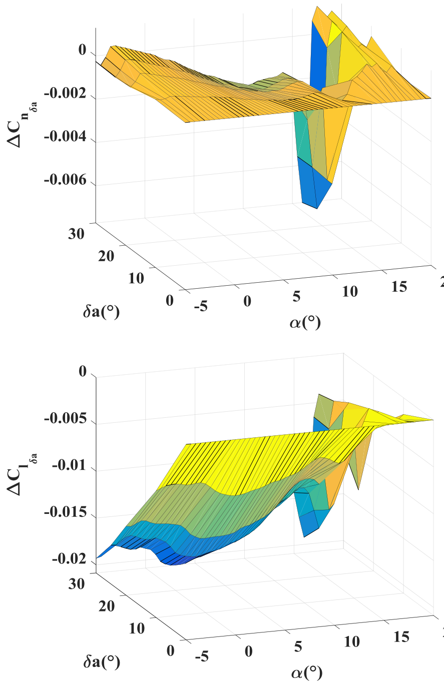

**FIGURE 7.** Increment of lateral-directional coefficients for $\delta_a$ at $\beta = 0^o$.

$\hat{C}_{n_r}$ can be approximated to be a constant of small negative magnitude (about $-0.005$) for $-4° \leq \alpha \leq 10°$, and then go up to be positive at higher $\alpha$. This reveals that the dynamic stability of yaw is quite weak. On the other hand, the coupling derivative $\hat{C}_{n_p}$ is adverse to yaw for $-3.7° \leq \alpha \leq 14.5°$. Compared with yaw, the dynamic stability of roll $\hat{C}_{l_p}$ is much better, except for $16° \leq \alpha \leq 18°$. Moreover, a favorable coupling derivative $\hat{C}_{l_r}$ is observed. The influence of amplitudes and frequency in the forced-oscillation tests is also presented in Fig.5 with the colored zones, which can be taken as the modeling uncertainties.

The incremental yaw and roll moments versus positive surface deflections and $\alpha$ for $\beta = 0°$ are respectively presented in Fig. 6 and Fig. 7. Both the rudder $\delta_r$ and aileron $\delta_a$ are efficient for $\alpha \leq 12°$, while rapid decrease and reversal in efficiency is observed at higher $\alpha$ probably due to flow separation. Besides, one can find that the rudder is inefficient for small deflections and the secondary effect of rudder deflection on the roll moment is noticeable.

The influence of the wingtips are evaluated with respect to $\alpha$ and $\beta$. It is found in the experiment that negative deflections of wingtips are more efficient for improving yaw stability than positive deflections. When the wingtips are fixed at $-40°$, the related increment of lateral-directional coefficients are shown in Fig. 8. One can see that restoring yaw moments with respect to $\beta$ are obtained with small nonlinearity to $\alpha$ before stall, whereas the dihedral effectiveness is somewhat sacrificed.

Normally, the nonlinear aerodynamic characteristics are captured in conventional wind tunnel tests and stored in look-up tables. Subsequently, the dimensionless aerodynamic coefficients in Eq. (4) corresponding to the real-time flight states can be determined through table lookup and data interpolation.

### C. MISALIGNMENT AND FRICTION MODELING

Misalignment moments are linked to the fact that the rotational center of the spherical joint differs from the CG of the aircraft model, which coincides with the applying point of aerodynamic forces $F_a$ in this case. As a result, the misalignment induced moments notably depend on the amount of

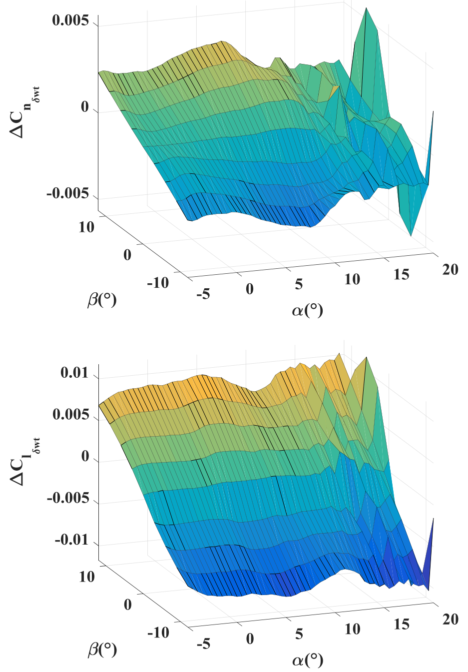

**FIGURE 8.** **Increment of lateral-directional coefficients for $\delta_{wt} = -40°$.**

misalignment $\Delta_{cg} = [\Delta x \ \Delta y \ \Delta z]^T$ in body-fixed coordinate.

$$\begin{bmatrix} L_{cg} \\ M_{cg} \\ N_{cg} \end{bmatrix} = \Delta_{cg} \times \left( \begin{bmatrix} -mg\sin\theta \\ mg\sin\phi\cos\theta \\ mg\cos\phi\cos\theta \end{bmatrix} + \begin{bmatrix} F_{ax} \\ F_{ay} \\ F_{az} \end{bmatrix} \right) \tag{5}$$

Similar to the aerodynamic moments, $F_{\mathrm{a}}$ is directly proportional to the aerodynamic force coefficients which is omitted here.

Friction moments resulting from the spherical joint are assumed to be a sum of dry and viscous frictions as in Ref. [18].

$$\begin{aligned} L_f &= -k_{1x} sign(p) - k_{2x} p \\ M_f &= -k_{1y} sign(q) - k_{2y} q \\ N_f &= -k_{1z} sign(r) - k_{2z} r \end{aligned} \tag{6}$$

Roll, pitch and yaw oscillations on a spring suspension are recorded for identification of the friction coefficients as detailed in Ref. [21].

## IV. FLIGHT DYNAMICS ANALYSIS AND COMPARISON

On the feasibility of the 3DOF rig in the wind tunnel to study the lateral-directional control of the tailless aircraft, comparison and analysis of flight dynamics between the 6-DOF free flight and the 3-DOF semi-free flight are carried out, including the trimming and modal characteristics. The influence of friction and misalignment, induced by the spherical joint, is studied as well.

Here, the constrained bifurcation analysis (CBA) approach [24]–[27] and publicly available Continuation Core and Toolboxes (COCO) [27] are incorporated into the trimming and stability investigation. The basis of CBA is to find the equilibriums, i.e. solutions to the following state and constraint (straight and level flight) equations [28]:

$$\dot{x} = f(x, u, P) \tag{7}$$

$$y = g(x) = 0, \quad y = [\gamma, \beta, \phi] \tag{8}$$

where $x = [V, \alpha, \beta, p, q, r, \theta, \phi]$ is the vector of state variables, $u = \delta_e$ is the continuation parameter, and $P = \left[\delta_{th}, \delta_a, \delta_r, X_{cg}, \delta_{r0}, \delta_{Wt}\right]$ represents the system parameters ($X_{cg}$ is the location of aircraft CG refers to the mean aerodynamic chord, $\delta_{r0}$ denotes pre-deflection for both of the left and right SDR). For 6-DOF free flight, the dynamic equations of states in Eq. (7) are taken from Ref. [23]; while for 3-DOF semi-free flight on the rig, the Eq. (7) is depicted in detail as Eq. (1) of this paper. Corresponding to the three constraints in Eq. (8), the parameters of $\delta_{th}$, $\delta_a$ and $\delta_r$ are freed for trimming, while the parameters of $\delta_{r0}$ and $\delta_{wt}$ are fixed for each flight configuration (cfg1: $\delta_{r0} = 0°$, $\delta_{wt} = 0°$; cfg2: $\delta_{r0} = 12°$, $\delta_{wt} = 0°$; cfg3: $\delta_{r0} = 0°$, $\delta_{wt} = -40°$). It should be pointed out that the state $V$ remains at the airspeed of the wind tunnel (30 m/s) and the throttle $\delta_{th}$ is fixed at zero during the continuation for 3-DOF semi-free flight.

Herein, it is important to mention that both the longitudinal and lateral-directional channels are trimmed and analyzed at the same time via continuation with the parameter $u = \delta_e$. From a lateral-directional flight dynamics point of view, one is most interested in the evolution of eigenvalues related to the states of $[\beta, p, r, \phi]$ along the attainable $\alpha$. However, the trimmed values of $[\beta, p, r, \phi]$ turn out to be zero throughout the continuation due to aerodynamic symmetry of the aircraft. As a result, the diagrams for $[\beta, p, r, \phi]$ with respect to the continuation parameter are not presented. Instead, the trimmed $\alpha$ is plotted as a function of $\delta_e$ with supplemental lateral-directional stability information, which is obtained by inspecting the eigenvalues corresponding to the states of $[\beta, p, r, \phi]$ along the equilibrium curves. Bifurcation plots obtained from the CBA continuation for the three aircraft configurations with the same $X_{cg} = 25\%$ are presented in Fig. 9. The saddle and Hopf bifurcation points indicate a single real pole or a pair of conjugate complex poles crossing the imaginary axis respectively. In the bifurcation diagram of 6-DOF free flight, three are two Hopf bifurcation points at $(\alpha, \delta \ \mathrm{e}) = (6.7°, -1.74°)$ and $(7.82°, -2.73°)$ in the curve of cfg1, resulting in the onset of a stable section. It can be inferred that the lateral-directional instability of the tailless aircraft is mainly related to unstable Dutch-roll mode due to a resultant decrease of $C_{n_\beta}$. To assess the effectiveness of $\delta_{r0}$ and $\delta_{Wt}$ for lateral-directional stability, continuations of the cfg2 and cfg3 are also plotted in Fig.9. One can note that aerodynamic benefits for yaw of the cfg2 and cfg3 are not sufficient to stabilize the lateral-directional channel, though the stability of the Dutch-roll mode, especially for the cfg3, may have been improved somewhat. For the three aircraft configurations, the bifurcation curves of 3-DOF semi-free flight show that the attainable range of $\alpha$ and the distribution of trimmed $\alpha$ with respect to $\delta_e$ are similar to that of 6-DOF free flight, except for the cfg3 at about $\alpha \in [0.2°, 2°]$.

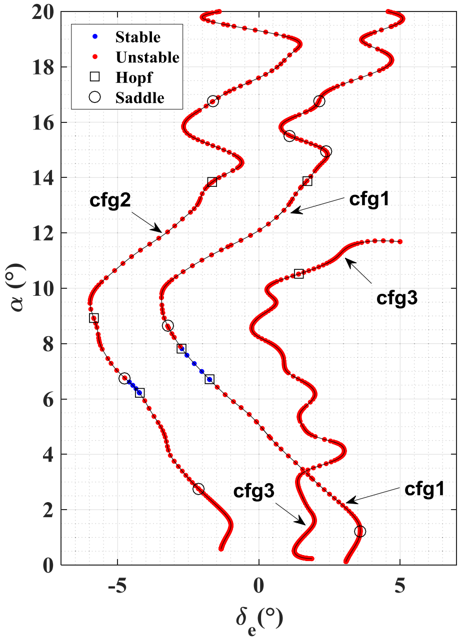

(a) 6-DOF

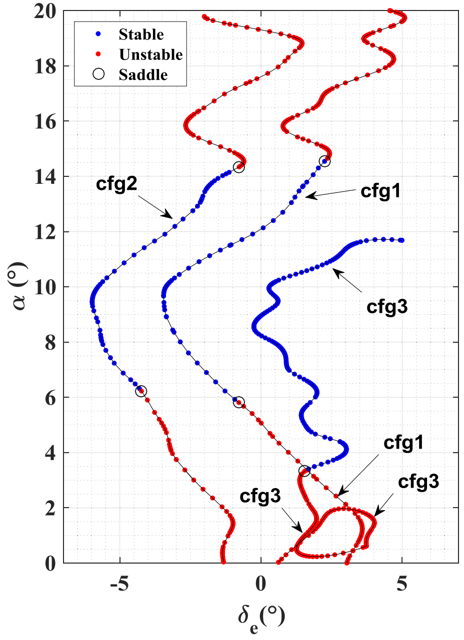

(b) 3-DOF

**FIGURE 9.** Comparison of CBA results between the 6-DOF free flight and the 3-DOF semi-free flight.

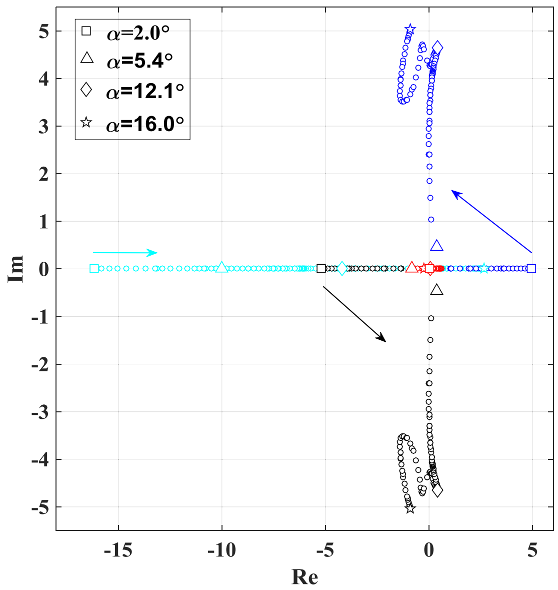

(a) 6-DOF

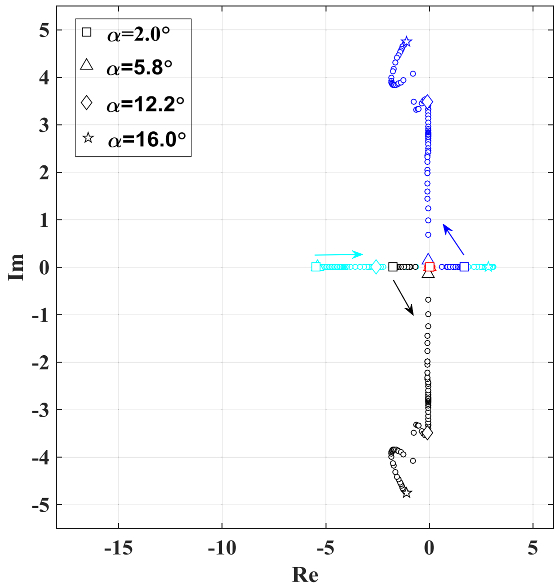

(b) 3-DOF

**FIGURE 10.** Comparison of lateral-directional modal characteristics between the 6-DOF free flight and the 3-DOF semi-free flight.

Meanwhile, it is noted that the stable sections of equilibrium points in the curves extend from $\alpha \in [6.7°, 7.8°]$ to [5.8°, 14.5° ] for the cfg1, from $\alpha \in [6.2°, 6.8°]$ to [6.2°, 14.3° ] for the cfg2 and from none to $\alpha \in [3.3°, 11.6°]$ for the cfg3. It seems that the lateral-directional stability of the tailless aircraft on the 3-DOF rig is significantly improved.

For more details about the improvement of the lateral-directional stability, the cfg1 is taken as an example for comparison of modal characteristics between the 6-DOF free flight and 3-DOF semi-free flight [29]. As shown in Fig.10, the eigenvalues corresponding to the states of $[\beta, p, r, \phi]$ are plotted with respect to $\alpha \in [2.0°, 16.0°]$. The selected section of $\alpha$ covers the conventional $\alpha$ range, which is mostly concerned by the researchers on the flight control. On one hand, the distribution and evolution of the poles with respect to $\alpha$ in Fig.10 (a) are similar to that in Fig.10 (b). At low $\alpha$, the Dutch-roll mode degrades to be two real poles, which move towards each other with the increase of $\alpha$ and then unite to be conjugate complex poles at $\alpha \approx 5.5°$. At medium $\alpha$, the natural frequency ($\omega_{nDR}$) of the Dutch-roll mode increases steadily until $\alpha \approx 12.0°$, while the damping ratio ($\zeta_{DR}$) remains at almost zero. However, compared with the 6-DOF free flight, $\zeta_{DR}$ of the 3-DOF case is slightly improved to be positive throughout the medium $\alpha$. It is that which results in the significant expansion of the stable section in Fig. 9(b).

**TABLE 2. Modification of the lateral-directional flying quality requirements.**

| Flying Quality Level | Full Scale (Dutch-roll & Roll Mode) | | | | 10% Scale (Dutch-roll & Roll Mode) | | | |
|---|---|---|---|---|---|---|---|---|
| | $\omega_{nDR}$ | $\zeta_{DR}$ | $\omega_{nDR}\cdot\zeta_{nDR}$ | $T_R$ | $\omega_{nDR}$ | $\zeta_{DR}$ | $\omega_{nDR}\cdot\zeta_{nDR}$ | $T_R$ |
| | rad/s | - | - | s | rad/s | - | - | s |
| 1 | $\geqslant$0.4 | $\geqslant$0.19 | $\geqslant$0.15 | $\leqslant$1.4 | $\geqslant$1.26 | $\geqslant$0.19 | $\geqslant$0.47 | $\leqslant$0.44 |
| 2 | $\geqslant$0.4 | $\geqslant$0.02 | $\geqslant$0.05 | $\leqslant$3.0 | $\geqslant$1.26 | $\geqslant$0.02 | $\geqslant$0.16 | $\leqslant$0.95 |
| 3 | $\geqslant$0.04 | $\geqslant$0.02 | - | $\leqslant$10.0 | $\geqslant$0.13 | $\geqslant$0.02 | - | $\leqslant$3.16 |

In the region of stall ($\alpha \approx 15.0^\circ$ ) and post-stall, the Dutch-roll mode demonstrates complicated evolution and the pole corresponding to the roll mode moves to the right half-plane. On the other hand, there are two main differences between the Fig.10 (a) and the Fig.10 (b). Firstly, the natural frequency of the Dutch-roll and roll mode in the 3-DOF case is lower, especially at low $\alpha$, because the airspeed is maintained at about 30 m/s by the wind tunnel while the trimmed airspeed in the 6-DOF free flight may be much higher at the same $\alpha$. Secondly, a pole locates at the origin for all $\alpha$ in the 3-DOF case due to the simplified motion of roll depicted as $\dot{\phi} = p$, which is derived from the Eq. (1g) for a straight level flight.

As the distribution and evolution of poles corresponding to the Dutch-roll and roll mode are key to describe the lateral-directional flight dynamics with respect to $\alpha$, it can be concluded that the lateral-directional flight dynamics of the tailless aircraft model on the 3-DOF rig are similar to that of the 6-DOF free flight based on the aforementioned analysis.

Furthermore, the dynamic influence of friction and misalignment introduced by the spherical joint is examined via simulation with the same doublet excitations (roll at 10s, yaw at 40s) using the yaw augmented ($K_\beta = -3, K_r = 1$) 3-DOF nonlinear model of cfg1 at $\alpha = 5^\circ$. It is observed that the friction improves the roll and yaw damping slightly but is negligible, while the misalignment may lead to serious corruption of dynamic similarity. As presented in Fig. 11, a small shift of aircraft model's CG along the longitudinal axis (especially for a rearward shift of $\Delta_x = -1$ mm) causes considerable differences in the transient responses of roll and yaw rate. Subsequently, the roll $\phi$ shifts a lot, and the sideslip $\beta$ shifts somewhat during the maneuvers. Hence, it's critical to modify CG of the aircraft model to coincide well with the spherical joint's center along the longitudinal axis as much as possible in 3-DOF semi-free flight tests.

## V. CONTROL LAW DESIGN

For control law design, the linear lateral-directional dynamics are obtained by linearizing and decoupling the 6-DOF nonlinear equations in Ref. [23] in steady wing-level condition (trimming airspeed $V_e$ and pitch angle $\theta_e$), resulting in the state space form in Eq. (9) with the states as $x_{lat} = [\beta, p, r, \phi]^T$. Moreover, the side force $Y$ and the moments $L$, $N$ are assumed to be linear functions of $\beta$, $p$, $r$ and inputs $u_{lat} = [\delta_a, \delta_r]^T$. According to the evolution of lateral-directional modal characteristics with respect to $\alpha$ in Fig. 10, the medium $\alpha = 7.5^\circ$ is selected to represent the open-loop flight dynamics.

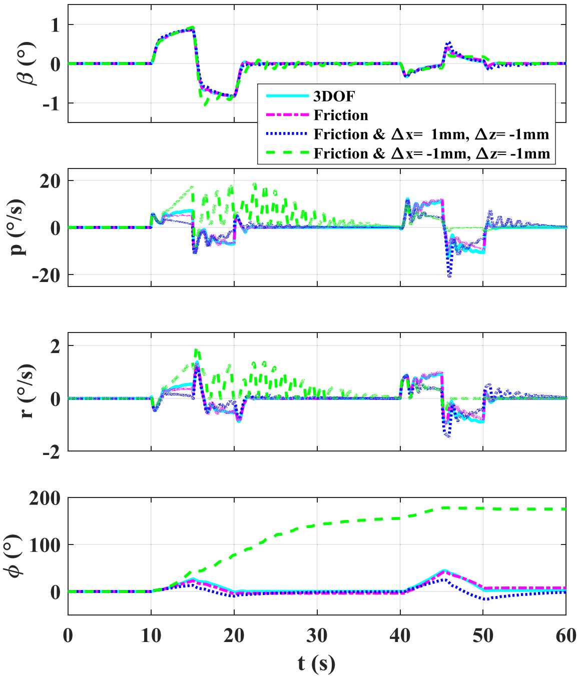

**FIGURE 11. Influence of friction and misalignment.**

To ensure that the control laws are representative of those applicable to the full scale piloted aircraft, both flying qualities and robustness have to be addressed. However, the flying quality specifications in Ref. [30], [31] can't be directly applied to a dynamically scaled aircraft model before being shifted to sub-scale one account for scale effects [32]. As the tailless demonstrator studied in this paper is a Class III aircraft in flight phase of category B, the criteria for evaluation of lateral-directional flying qualities are adopted from the Ref. [23], [31], and the required indicators of the Dutch-roll and roll mode are specified in Table 2. One can note that the lower bound of the Dutch-roll mode frequency requirement $\omega_{nDR}$ is modified by multiplying a scaled response value $1\big/\sqrt{K_L}$, while the damping ratio should be applied directly because of non-dimensional. Similarly, the upper bound of the roll mode time constant $T_R$ is modified by multiplying $\sqrt{K_L}$.

Towards uncertainties lying in aerodynamic interference of the rig and fabrication error of the aircraft model, the guidelines of 6dB Gain Margin and 45° Phase Margin from the MIL-F-9490D [33] are examined during the development of control laws.

A simplified block diagram of the lateral-directional control law developed with the EA [34], [35] control technique is shown in Fig. 12. The lateral stick commands the roll rate and the pedal commands the yaw rate. The linear aircraft plant $\Sigma_{lat}$ depicted in Eq. (9), as shown at the bottom of this page, is augmented with an integrator for each controlled variable to reduce tracking error and provide robustness. The washout filter is fixed as a first-order unit. As a result, the determination of the control gains can be viewed as a static output feedback problem described in Eq. (10), as shown at the bottom of this page. In which $X_\beta$ is the washout filter state, $X_{Ip}$ and $X_{Ir}$ are the integrator states, and $A_{11}$ is elaborated in Eq. (11), as shown at the bottom of this page.

The desired closed-loop eigenvalues $\lambda_d$ in Eq. (12), as shown at the bottom of this page, and the matching eigenvectors $V_d$ in Eq. (13) associated with flight modes are chosen to meet level 1 requirements in Table 2.

$$\mathrm{V_d}=\begin{array}{c}\left[\begin{array}{cccccc}\multicolumn{2}{c}{\overbrace{\text{Dutch}-\text{roll}}} & \text{roll} & \text{spiral} & \multicolumn{2}{c}{\overbrace{\text{integral}}}\\ 1 & \times & 0 & 0 & 0 & \times\\ \times & \times & 1 & \times & \times & 0\\ \times & 1 & \times & \times & \times & \times\\ 0 & 0 & \times & 1 & \times & \times\\ \times & \times & \times & \times & \times & \times\\ \times & \times & \times & \times & 1 & \times\\ \times & \times & \times & \times & \times & 1\end{array}\right]\end{array}\begin{array}{c}\\ \beta\\ \mathrm{p}\\ \mathrm{r}\\ \mathrm{f}\\ \mathrm{x}_\beta\\ \mathrm{x_{Ip}}\\ \mathrm{x_{Ir}}\end{array}\tag{13}$$

where “0” and “1” denotes hard constraint eigenvectors and “× ” denotes arbitrary element.

The feedback control law employs the following form:

$$u_{lat}=K_{lat}\cdot y_{lat}\tag{14}$$

where

$$u_{lat}=\begin{bmatrix}\delta_a & \delta_r\end{bmatrix}^T,$$
$$y_{lat}=\begin{bmatrix}p & r & x_\beta & x_{I_p} & x_{I_r}\end{bmatrix}^T.$$

---

$$\Sigma_{\mathrm{lat}}:\begin{cases}\dot{\mathrm{x}}_{\mathrm{lat}}=\underbrace{\begin{bmatrix}\mathrm{Y/V_e} & \sin\alpha & -\cos\alpha & \mathrm{g}\cos\theta_{\mathrm{e}}\\ \mathrm{L}_\beta & \mathrm{L_p} & \mathrm{L_r} & 0\\ \mathrm{N}_\beta & \mathrm{N_p} & \mathrm{N_r} & 0\\ 0 & 1 & \tan\theta_{\mathrm{e}} & 0\end{bmatrix}}_{\mathrm{A_{lat}}}\mathrm{x_{lat}}+\underbrace{\begin{bmatrix}\mathrm{Y}_{\delta_\mathrm{a}}/\mathrm{V_e} & \mathrm{Y}_{\delta_\mathrm{r}}/\mathrm{V_e}\\ \mathrm{L}_{\delta_\mathrm{a}} & \mathrm{L}_{\delta_\mathrm{r}}\\ \mathrm{N}_{\delta_\mathrm{a}} & \mathrm{N}_{\delta_\mathrm{r}}\\ 0 & 0\end{bmatrix}}_{\mathrm{B_{lat}}}\mathrm{u_{lat}}\\ \mathrm{y_{lat}}=\underbrace{\begin{bmatrix}1 & 0 & 0 & 0\\ 0 & 1 & 0 & 0\\ 0 & 0 & 1 & 0\end{bmatrix}}_{\mathrm{C_{lat}}}\mathrm{x_{lat}}\end{cases}\tag{9}$$

$$\begin{cases}\begin{bmatrix}\dot{\mathrm{x}}_{\mathrm{lat}}\\ \dot{\mathrm{x}}_\beta\\ \dot{\mathrm{x}}_{\mathrm{Ip}}\\ \dot{\mathrm{x}}_{\mathrm{Ir}}\end{bmatrix}=\underbrace{\begin{bmatrix}\mathrm{A_{11}} & -\mathrm{K}_\beta\mathrm{B_{lat}}(:,2) & \mathrm{K_{Ip}B_{lat}}(:,1) & \mathrm{K_{Ir}B_{lat}}(:,2)\\ -\mathrm{z_{wo}C_{lat}}(1,:) & -\mathrm{z_{wo}} & 0 & 0\\ -\mathrm{C_{lat}}(2,:) & 0 & 0 & 0\\ -\mathrm{C_{lat}}(3,:) & 0 & 0 & 0\end{bmatrix}}_{\mathrm{A}_{\mathrm{lat}\_cl}}\begin{bmatrix}\mathrm{x_{lat}}\\ \mathrm{x}_\beta\\ \mathrm{x_{Ip}}\\ \mathrm{x_{Ir}}\end{bmatrix}\\ \qquad+\underbrace{\begin{bmatrix}(\mathrm{K_p}+\mathrm{K_{ff\_p}})\mathrm{B_{lat}}(1,:) & (\mathrm{K_r}+\mathrm{K_{ff\_r}})\mathrm{B_{lat}}(2,:)\\ 0 & 0\\ 1 & 0\\ 0 & 1\end{bmatrix}}_{\mathrm{B_{lat\_cl}}}\begin{bmatrix}\mathrm{p_{ref}}\\ \mathrm{r_{ref}}\end{bmatrix}\\ \begin{bmatrix}\mathrm{p}\\ \mathrm{r}\\ \mathrm{x}_\beta\\ \mathrm{x_{Ip}}\\ \mathrm{x_{Ir}}\end{bmatrix}=\underbrace{\begin{bmatrix}\mathrm{C_{lat}}(2:3,:) & \mathrm{zeros}(2,3)\\ \mathrm{zeros}(4,4) & \mathrm{eye}(3,3)\end{bmatrix}}_{\mathrm{C_{lat\_cl}}}\begin{bmatrix}\mathrm{x_{lat}}\\ \mathrm{x}_\beta\\ \mathrm{x_{Ip}}\\ \mathrm{x_{Ir}}\end{bmatrix}\end{cases}\tag{10}$$

$$\mathrm{A_{11}}=\mathrm{A_{lat}}-\mathrm{K}_\beta\mathrm{B_{lat}}(:,2)\mathrm{C_{lat}}(1,:)-\mathrm{K_pB_{lat}}(:,1)\mathrm{C_{lat}}(2,:)-\mathrm{K_rB_{lat}}(:,2)\mathrm{C_{lat}}(3,:)\tag{11}$$

$$\lambda_d=[\underbrace{-1.5+1.5\mathrm{i}\quad -1.5-1.5\mathrm{i}}_{\text{Dutch}-\text{roll}}\quad\underbrace{-8}_{\text{roll subsidence}}\quad\underbrace{-0.01}_{\text{spiral}}\quad\underbrace{-0.3\quad -0.3}_{\text{integral}}]\tag{12}$$

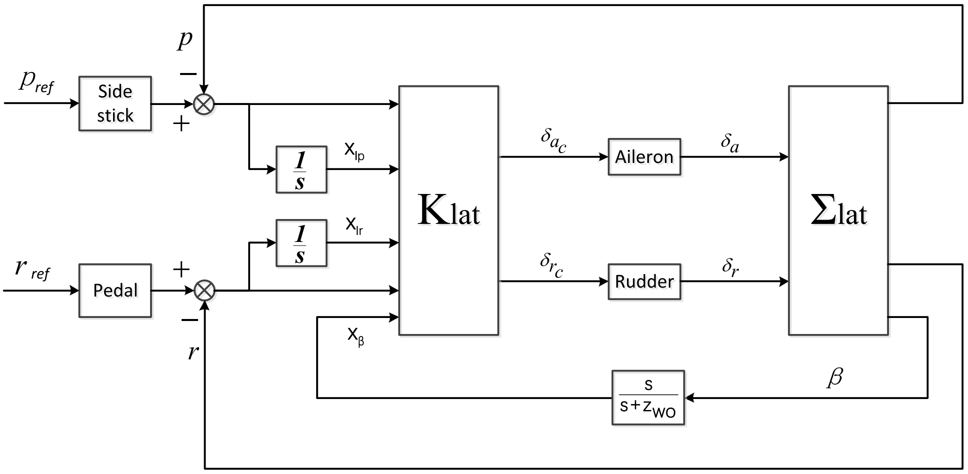

**FIGURE 12.** Layout of lateral-directional control law.

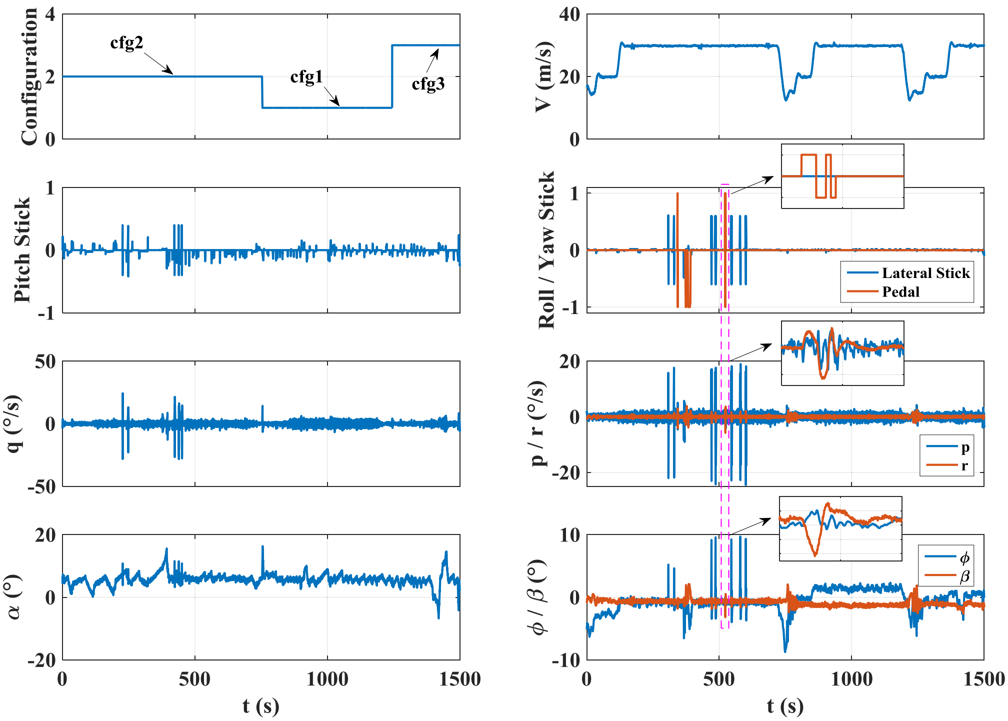

**FIGURE 13.** Closed-loop test scenario of the three aircraft configurations on the 3-DOF rig.

The feedback controller $K_{lat}$ is then synthesized using the eigenstructure assignment algorithm in Ref. [36], and the obtained gain matrix is as following:

$$K_{lat} = \begin{bmatrix} -0.0226 & 0.4895 & 3.2116 & -0.1768 & 0.2803 \\ 0.4821 & -2.7445 & 0.2000 & 0.4996 & -0.1226 \end{bmatrix} \quad (15)$$

The closed-loop eigenvalues are presented in Fig. 14 along with the open-loop eigenvalues. One can find that the desired closed-loop modal characteristics specified in Eq. (12) have been achieved.

## VI. EXPERIMENTAL VALIDATION AND EVALUATION

To validate and evaluate the designed control laws, a series of semi-free flight tests have been conducted with the PIL experimental setup introduced in Sec. II of this paper. The experimental contents are outlined in Table 3 and the results are discussed in this section.

### A. VALIDATION OF CONTROL LAW

A flight test scenario is conducted for the aforementioned three configurations of aircraft model on the 3-DOF rig in the FL-14 wind tunnel. The scenario involves flying the aircraft model at various combinations of configuration, airspeed and

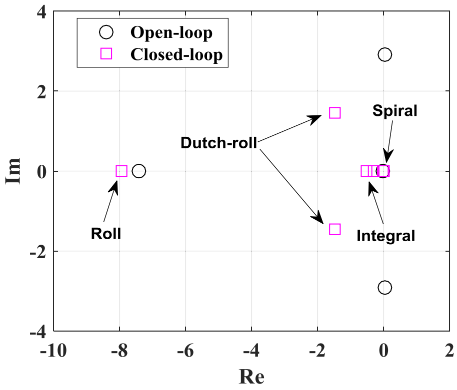

**FIGURE 14.** Comparison of the eigenvalues between the open-loop system and closed-loop system.

**TABLE 3.** Outline of the semi-free flight tests.

| Test setting | Validation | Evaluation |
|---|---|---|
| Aircraft configuration | cfg1, cfg2, cfg3 | cfg1, cfg2, cfg3 |
| Airspeed (m/s) | 15～20～30 | 30 |
| Angle of attack (°) | 0～15 | 4, 8, 10, 12 |
| Handling excitation | Pilot handling, Multistep sequences | Multistep '3-2-1-1' |

$\alpha$ using pilot manipulations, which have been normalized to the non-dimensional value of $[-1\ 1]$.

The flight parameters, stick inputs and configuration settings are recorded and presented in Fig. 13. The flight test scenario begins with 'cfg2' and then switched to 'cfg1' and 'cfg3' at the time of 755s and 1245s respectively, where notable disturbances are observed to be suppressed rapidly. For safety, the aircraft configuration and corresponding control law are switched rapidly via the flight computer at the airspeed of about 15 m/s. For each configuration, adequate robustness of the control system is assessed at three airspeed increments (15 m/s, 20 m/s and 30 m/s) covering low to moderate $\alpha$. From the time history of the lateral stick and pedal, one can note that little manual intervention is imposed to maintain the angles of $\beta$ and $\phi$ at almost zero while nosing up and down. Besides, the pilot rating indicates a good handling response and an acceptable workload throughout the test scenario. Moreover, the multistep input sequences, such as doublet, '3-2-1-1' and chirp swept, are also applied to test the performance of reference command tracking. Thus, the test scenario validates the design of control laws that succeed to improve the stability and controllability of the tailless aircraft.

### *B. EVALUATION OF FLYING QUALITIES*

To evaluate the lateral-directional flying qualities, a period of 2.8s '3-2-1-1' multistep input is applied to the pedal ($\eta_r$) and lateral stick ($\eta_a$) simultaneously for adequate $\beta$ and $\phi$ response respectively, while decreasing the adverse coupling as much as possible. The low order equivalent system (LOES) approach in Ref [37], [38] is introduced to characterize the closed-loop dynamic response of the control augmented aircraft model. Following a standard approach [37], the model structure for LEOS modeling is fixed a priori in Eq. (16) to correspond to classical linear aircraft response with an input delay ($\tau_\beta,\ \tau_\phi$), the problem reduces to parameter estimation based on measured data.

$$\begin{cases} \dfrac{\beta(s)}{\eta_r(s)} \\ = \dfrac{K_{\beta 0}\left(s+1/T_{\beta 1}\right)\left(s+1/T_{\beta 2}\right)\left(s+1/T_{\beta 3}\right)}{\left(s+1/T_R\right)\left(s+1/T_S\right)\left(s^2+2\zeta_{DR}\omega_{nDR}s+1/T_{\beta 1}\right)}e^{-\tau_\beta s} \\ \dfrac{\phi(s)}{\eta_a(s)} \\ = \dfrac{K_{\phi 0}\left(s^2+2\zeta_\phi\omega_\phi s+\omega_\phi^2\right)}{\left(s+1/T_R\right)\left(s+1/T_S\right)\left(s^2+2\zeta_{DR}\omega_{nDR}s+\omega_{nDR}^2\right)}e^{-\tau_\phi s} \end{cases}$$

Parameter estimation is performed in the frequency domain using the integrated equation-error and output-error approach as in Ref. [37]. Input-output data are measured at a sampling rate of 100Hz and transformed into the frequency domain using the Fourier transform. Parameters in Eq. (16) are identified in the interval [0.1 10] rad/s with a resolution of 0.1 rad/s to cover the model dynamics of interest and the frequency band of typical pilot inputs. As shown in Fig. 15, the LEOS models fit well to the measured data both in frequency and time domain, indicating that the identified LEOS model is adequate to capture the lateral-directional dynamics of the control augmented aircraft model.

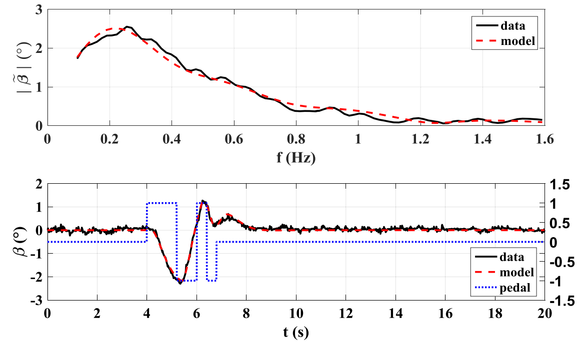

(a) sideslip

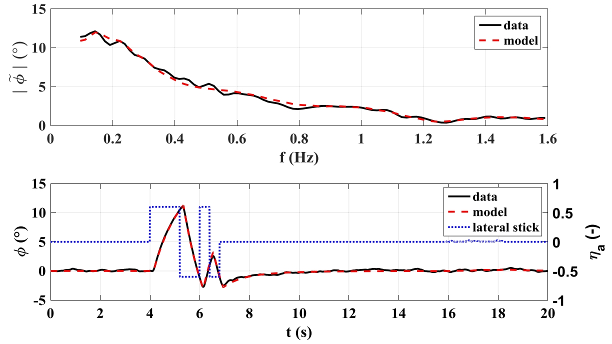

(b) bank angle

**FIGURE 15.** LEOS model fit to $\beta$ and $\phi$ for 3-2-1-1 maneuver.

The key lateral-directional flying qualities of the aircraft model on the 3-DOF rig are expressed by the Dutch-roll frequency $\omega_{nDR}$, the damping ratio $\zeta_{nDR}$ and the roll mode time

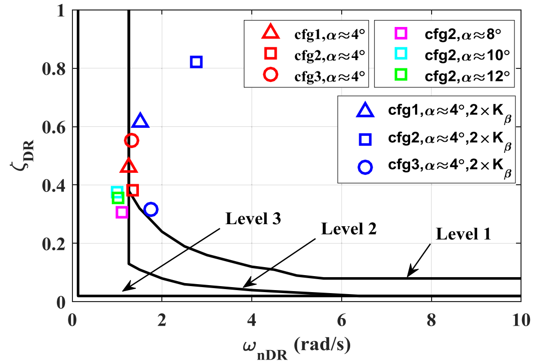

(a) Dutch-roll mode

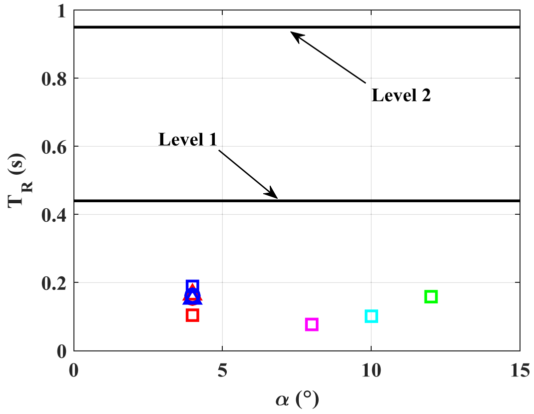

(b) roll mode

**FIGURE 16.** Lateral-directional flying qualities of the control augmented aircraft model.

constant $T_R$. These flying quality parameters are calculated from the identified LEOS model-derived parameters for various combinations of aircraft configuration, angle of attack and controller gain of sideslip ($K_\beta$). The results are plotted in Fig. 16 against the modified criterion of lateral-directional flying qualities in Table. 2. As can be seen from the diagram of Fig. 16 (a), the $\omega_{nDR} \cdot \zeta_{nDR}$ value is very close to the lower criterion boundary of level 1 at $\alpha \approx 4°$ for each configuration, indicating that the goals of control law design have been achieved. The 'cfg2' is selected for comparison at higher $\alpha$ of 8°, 10° and 12°, where the Dutch roll mode flying quality corrupts to level 3 due to insufficient Dutch-roll frequency $\omega_{nDR}$. It is noted that the yaw attitude response quickness can be remarkably improved with double increases of sideslip gains ($K_\beta$), therefore, simultaneously, validating the desired 6 dB gain margin [39]. Whereas the variation tendency of the corresponding damping ratio is unpredictable for unmodified control gains of yaw rate. However, it's important to recall that too much increase of feedback gain is not preferable for stability and robustness especially at high $\alpha$. As demonstrated in the diagram of Fig. 16 (b), the roll mode characteristics in terms of the time constant values $T_R$ meet level 1 for all the tested conditions.

Obviously, the lateral-directional flying qualities of the tailless demonstrator mainly suffer from insufficient natural frequency of the Dutch-roll mode, which could be improved to level 1 with sufficient sideslip feedback. However, a refinement of the controller gains is essential to achieve level 1 Dutch-roll mode through the tested range of $\alpha$, and the adverse influence of large sideslip feedback gains to the closed-loop performance should be further investigated in the future.

## VII. CONCLUSION

In this paper, physical simulation of flight dynamics and validation of control laws have been carried out for a 10% scaled tailless aircraft model using the 3-DOF dynamic rig in the FL-14 wind tunnel. An overview of the tailless aircraft configurations and a semi-free flight related experimental setup are introduced and then a suitable nonlinear mathematical model of flight dynamics on the rig is presented considering friction and misalignment. An important aspect of modeling is the establishment of an aerodynamic model with data from static and dynamic wind tunnel tests, which reveals challenging yaw stability and control. From a point of modal characteristics view, the open-loop instability mainly results from the Dutch-roll mode with negative or very poor damping ratio, which degreed to be a pair of real poles at low $\alpha$. Besides, the pole of roll mode moves rapidly towards the origin with the increase of $\alpha$ and becomes unstable in the stall region.

The detailed trimming and stability characteristics of the tailless aircraft is calculated and analyzed with the CBA method for comparison between the 3-DOF semi-free flight and the 6-DOF free flight. It is discussed that the differences of lateral-directional flight dynamics mainly result from the 3-DOF test settings of constant airspeed and constrained translational motions in the wind tunnel. Although the tighter distribution of the four poles at low $\alpha$ and slightly damp improved Dutch-roll mode at medium $\alpha$ are observed for the case of 3-DOF semi-free flight, the overall modal distribution and evolution with respect to $\alpha$ is similar to that of the 6-DOF free flight. Further, the influence of friction and misalignment induced by the rig is investigated using a nonlinear simulation of yaw augmented 3-DOF aircraft model, indicating that the misalignment should be eliminated as much as possible.

Control laws are designed to stabilize the attitude of the aircraft model and improve flying qualities to level 1 of the scale modified criteria using the EA control technique, and then implemented in 3-DOF semi-free flight tests in the FL-14 wind tunnel. A test scenario with pilot manipulation verifies the satisfactory stability and robustness of the closed-loop system for three aircraft configurations with respect to various combinations of airspeed and angle of attack. To evaluate the actual flying qualities, LOES models are identified from 3-2-1-1 maneuvers of the yaw and roll axis. As indicated by the presented results, the tailless aircraft model's flying qualities meet level 1 requirements in terms of Dutch-roll and roll mode at $\alpha \approx 4°$ for the three configurations. However, with the increase of $\alpha$, the flying quality parameter $\omega_{nDR} \cdot \zeta_{nDR}$ decreases to Level 3, which might be improved with larger feedback gains of sideslip and yaw rate in the future tests.

## REFERENCES

[1] R. Colgren and R. Loschke, "Effective design of highly maneuverable tailless aircraft," *J. Aircr.*, vol. 45, no. 4, pp. 1441–1449, Jul. 2008.

[2] R. H. Liebeck, "Design of the blended wing body subsonic transport," *J. Aircr.*, vol. 41, no. 1, pp. 10–25, Jan. 2004.

[3] J. Bowlus, D. Multhopp, S. Banda, J. Bowlus, D. Multhopp, and S. Banda, "Challenges and opportunities in tailless aircraft stability and control," in *Proc. Guid., Navigat., Control Conf.*, Aug. 1997, p. 3830.

[4] S. J. Woolvin, "UCAV configuration & performance trade-offs," in *Proc. 44th AIAA Aerosp. Sci. Meeting Exhib.*, 2006, p. 1264.

[5] C. M. Meckstroth and W. B. Blake, "Control focused multidisciplinary design optimization of tailless fighter aircraft," in *Proc. 16th AIAA/ISSMO Multidisciplinary Anal. Optim. Conf.*, Jun. 2015, p. 2324.

[6] D. D. Vicroy, T. D. Loeser, and A. Schütte, "Static and forced-oscillation tests of a generic unmanned combat air vehicle," *J. Aircraft*, vol. 49, no. 6, pp. 1558–1583, 2012.

[7] R. M. Cummings and A. Schütte, "Integrated computational/experimental approach to unmanned combat air vehicle stability and control estimation," *J. Aircr.*, vol. 49, no. 6, pp. 1542–1557, Nov. 2012.

[8] J. Park, J.-Y. Choi, Y. Jo, and S. Choi, "Stability and control of tailless aircraft using variable-fidelity aerodynamic analysis," *J. Aircr.*, vol. 54, no. 6, pp. 2148–2164, Nov. 2017.

[9] A. Schütte, K. C. Huber, N. T. Frink, and O. J. Boelens, "Stability and control investigations of generic 53 degree swept wing with control surfaces," *J. Aircr.*, vol. 55, no. 2, pp. 502–533, Mar. 2018.

[10] S. Hitzel and D. Zimper, "Wind tunnel, simulation, and 'real' flight of advanced combat aircraft: Industrial perspective," *J. Aircr.*, vol. 55, no. 2, pp. 587–602, Mar. 2018.

[11] J. Schwithal, D. Rohlf, G. Looye, and C. M. Liersch, "An innovative route from wind tunnel experiments to flight dynamics analysis for a highly swept flying wing," *CEAS Aeronaut. J.*, vol. 7, no. 4, pp. 645–662, Dec. 2016.

[12] G. Stenfelt and U. Ringertz, "Yaw control of a tailless aircraft configuration," *J. Aircr.*, vol. 47, no. 5, pp. 1807–1811, Sep. 2010.

[13] G. Stenfelt and U. Ringertz, "Yaw departure and recovery of a tailless aircraft configuration," *J. Aircr.*, vol. 50, no. 1, pp. 311–315, Jan. 2013.

[14] G. Stenfelt and U. Ringertz, "Lateral stability and control of a tailless aircraft configuration," *J. Aircr.*, vol. 46, no. 6, pp. 2161–2164, Nov. 2009.

[15] D. Vicroy, "Blended-wing-body low-speed flight dynamics: Summary of ground tests and sample results," in *Proc. 47th AIAA Aerosp. Sci. Meeting Including New Horizons Forum Aerosp. Expo.*, Jan. 2009, p. 933.

[16] E. B. Jackson and C. W. Buttrill, "Control laws for a wind tunnel free-flight study of a blended-wing-body aircraft," NASA Langley Res. Center, Hampton, VA, USA, Tech. Rep. NASA/TM-2006-214501, Aug. 2006.

[17] Z. Gong, S. Araujo-Estrada, M. H. Lowenberg, S. A. Neild, and M. G. Goman, "Experimental investigation of aerodynamic hysteresis using a five-degree-of-freedom wind-tunnel maneuver rig," *J. Aircr.*, vol. 56, no. 3, pp. 1029–1039, May 2019.

[18] D. I. Ignatyev, M. E. Sidoryuk, K. A. Kolinko, and A. N. Khrabrov, "Dynamic rig for validation of control algorithms at high angles of attack," *J. Aircr.*, vol. 54, no. 5, pp. 1760–1771, Sep. 2017.

[19] J. Pattinson, M. H. Lowenberg, and M. G. Goman, "Multi-degree-of-freedom wind-tunnel maneuver rig for dynamic simulation and aerodynamic model identification," *J. Aircr.*, vol. 50, no. 2, pp. 551–566, Mar. 2013.

[20] G. Strub, S. Theodoulis, V. Gassmann, S. Dobre, and M. Basset, "Gain-scheduled autopilot design and validation for an experimental guided projectile prototype," *J. Guid., Control, Dyn.*, vol. 41, no. 2, pp. 461–475, 2018.

[21] L. Guo, M. Zhu, B. Nie, P. Kong, and C. Zhong, "Initial virtual flight test for a dynamically similar aircraft model with control augmentation system," *Chin. J. Aeronaut.*, vol. 30, no. 2, pp. 602–610, Apr. 2017.

[22] B. Nie, L. Guo, P. Kong, M. Jiang, and M. Zhu, "Hardware development of the wind tunnel based virtual flight system," in *Proc. IEEE Chin. Guid., Navigat. Control Conf.*, Aug. 2014, pp. 1135–1138.

[23] B. L. Stevens and F. L. Lewis, "Aircraft control and simulation," *Aircr. Eng. Aerosp. Technol.*, vol. 76, no. 5, pp. 142–376, Oct. 2004.

[24] M. G. Goman, G. I. Zagainov, and A. V. Khramtsovsky, "Application of bifurcation methods to nonlinear flight dynamics problems," *Prog. Aerosp. Sci.*, vol. 33, nos. 9–10, pp. 539–586, Jan. 1997.

[25] D. Wu, M. Chen, and H. Ye, "Analysis and recovery of aircraft deep-stall phenomena using bifurcation analysis," *IEEE Access*, vol. 8, pp. 29319–29333, 2020.

[26] A. K. Khatri, J. Singh, and N. K. Sinha, "Aircraft design using constrained bifurcation and continuation method," *J. Aircr.*, vol. 51, no. 5, pp. 1647–1653, Sep. 2014.

[27] H. Dankowicz and F. Schilder, *Recipes for Continuation*. Philadelphia, PA, USA: SIAM, 2013.

[28] N. Ananthkrishnan and N. K. Sinha, "Level flight trim and stability analysis using extended bifurcation and continuation procedure," *J. Guid., Control, Dyn.*, vol. 24, no. 6, pp. 1225–1228, Nov. 2001.

[29] A. N. Khrabrov, M. E. Sidoryuk, E. N. Kolesnikov, Y. A. Vinogradov, I. I. Grishin, and K. A. Kolinko, "On possibility of critical flight regime study in wind tunnels using three-degree-of-freedom gimbals," *TsAGI Sci. J.*, vol. 45, no. 8, pp. 825–839, 2014.

[30] *Flying Qualities of Piloted Aircraft*, document MIL-STD-1797A, Various, 1997.

[31] *Flying Qualities of Piloted Airplanes*, document MIL-F-8785C, United States Dep. Def., 1980.

[32] S. Sadovnitchii, V. Ryabkov, A. Rushenko, J. Sandoval, S. Sadovnitchii, V. Ryabkov, A. Rushenko, and J. Sandoval, "Modelling of aircraft flight by means of dynamically similar models with a flight control systems similarity," in *Proc. Modeling Simulation Technol. Conf.*, Aug. 1997, p. 3792.

[33] J. L. Townsend and P. E. Blatt, "New MIL-F-9490D requirements and implications on future flight control design," *J. Aircr.*, vol. 13, no. 9, pp. 670–675, Sep. 1976.

[34] C. Nieto-Wire and K. Sobel, "Flight control design for a tailless aircraft using eigenstructure assignment," *Int. J. Aerosp. Eng.*, vol. 2011, pp. 1–13, Jun. 2011.

[35] C. Nieto-Wire and K. Sobel, "Eigenstructure assignment for a tailless aircraft," in *Proc. AIAA Guid., Navigat. Control Conf. Exhib.*, Aug. 2007, p. 6417.

[36] J.-F. Magni, *Robust Modal Control With a Toolbox for Use With MATLAB*. Boston, MA, USA: Springer, 2002.

[37] V. Klein and E. A. Morelli, *Aircraft System Identification: Theory and Practice*. New York, NY, USA: AIAA, 2006.

[38] P. Huber, S. Weiss, and H. Galleithner, "X-31A initial flying qualities results using equivalent modeling flight test evaluation techniques," in *Proc. 18th Atmos. Flight Mech. Conf.*, Aug. 1991, p. 2891.

[39] T. Wendel, J. Boland, and D. Hahne, "High angle of attack control law development for a free-flight wind tunnel model using direct eigenstructure assignment," in *Proc. Navigat. Control Conf.*, Aug. 1991, p. 2627.

**BOWEN NIE** received the B.S. degree in automation from Northeastern University, in 2004, and the M.S. degree in control science and engineering from the National University of Defense Technology, in 2007, where he is currently pursuing the Ph.D. degree in control science and engineering.

He visited the GIPSA-Lab, Grenoble Alpes University, France, as an Academic Visitor, from 2017 to 2018. Since 2007, he has been a Research Assistant with the Low-Speed Aerodynamics Research Institute, China Aerodynamics Research and Development Center. His research interests include the integrated aerodynamic, control and flight investigation of novel aircraft in the low-speed wind tunnel, modeling of unsteady aerodynamics, and linear parameter varying systems.

**ZHITAO LIU** received the B.S. degree in aerodynamics from the National University of Defense Technology, in 2001, and the M.S. degree in fluid dynamics from CARDC, in 2004. He is currently an Aeronautical Scientist with the China Aerodynamics Research and Development Center. He is mainly involved in high angle of attack aerodynamics of aircraft, including high angle of attack test technique, flow visualization and control, unsteady aerodynamic modeling, and nonlinear flight dynamics. He has taken part in the development of a six-degree-of-freedom dynamic test rig and model free flight system in a large low-speed wind tunnel. He has published more than 40 academic articles and authorized eight patents.

**FEI CEN** received the B.Sc. degree in automation from Tsinghua University, in 2008, and the M.Sc. degree in aircraft design from the China Aerodynamics Research and Development Center, in 2011. He is currently pursuing the Ph.D. degree in control theory and control engineering with Tsinghua University. He was an Exchange Ph.D. Student with the Faculty of Aerospace Engineering, University of Bristol, U.K., from 2017 to 2018. Since 2008, he has been a Research Assistant with the Low-Speed Aerodynamics Research Institute, China Aerodynamics Research and Development Center. His principal research interests are nonlinear flight dynamics and control in general, including related wind tunnel experimentation, and in the use of bifurcation analysis to study nonlinear systems, such as flight dynamics under upset flight conditions and control strategies for loss-of-control prevention in particular.

**DUONENG LIU** received the M.S. degree in control science and engineering and the Ph.D. degree in aeronautical and astronautical science from the National University of Defense Technology (NUDT), China, in 2011 and 2016, respectively. He is currently a Research Assistant with the Low-Speed Aerodynamics Research Institute, China Aerodynamics Research and Development Center. His current research interests include flight dynamics, control, and trajectory planning and simulation for airplanes and aerial robots.

**HONGXU MA** received the B.S. degree in automatic control, the M.S. degree in intelligent control, and the Ph.D. degree in control science and control engineering from the National University of Defense Technology, in 1988, 1991, and 1995, respectively.

In 1995, he stayed in the school for research work. He is currently a Professor with the National University of Defense Technology. He is mainly involved in the research of foot robots. In 2000, he realized the dynamic walking of Chinese two-legged robots for the first time. He has published more than 150 high-level academic articles, published one monograph, and authorized more than ten patents.

**OLIVIER SENAME** received the Ph.D. degree from Ecole Centrale Nantes, in 1994. He is currently a Professor with the Institute Polytechnique de Grenoble within GIPSA-Lab. He is the (co)author of two books, 60 international journal articles, and more than 200 international conference papers. He has supervised 32 Ph.D. students. His main research interests include linear parameter varying systems and automotive applications. He was the General Chair of the IFAC Joint Conference SSSC-TDS-FDA 2013, of the 1st IFAC Workshop on Linear Parameter Varying Systems 2015. He was the IPC Chair of the 2nd IFAC Workshop LPVS 2018. He has led several industrial (Renault, Volvo Trucks, JTEKT, Delphi) and international (Mexico, Italy, Hungary) collaboration projects.

• • •